

## Problems in Radiation Detection and Measurement

Nuclear medicine studies are performed with a variety of types of radiation measurement instruments, depending on the kind of radiation source that is being measured and the type of information sought. For example, some instruments are designed for in vitro measurements on blood samples, urine specimens, and so forth. Others are designed for in vivo measurements of radioactivity in patients (Chapter 12). Still others are used to obtain images of radioactive distributions in patients (Chapters 13, 14, and 17-19).

All these instruments have special design characteristics to optimize them for their specific tasks, as described in the chapters indicated above; however, some considerations of design characteristics and performance limitations are common to all of them. An important consideration for any radiation measurement instrument is its *detection efficiency*. Maximum detection efficiency is desirable because one thus obtains maximum information with a minimum amount of radioactivity.

Also important are the instrument's *counting rate limitations*. There are finite counting rate limits for all counting and imaging instruments used in nuclear medicine, above which inaccurate results are obtained because of data losses and other data distortions. Non-penetrating radiations, such as  $\beta$  particles, have special detection and measurement problems. In this chapter, we discuss some of these general considerations in nuclear medicine instrumentation.

### A. DETECTION EFFICIENCY

#### 1. Components of Detection Efficiency

*Detection efficiency* refers to the efficiency with which a radiation-measuring instrument converts emissions from the radiation source into useful signals from the detector. Thus if a  $\gamma$ -ray-emitting source of activity  $A$  (Bq) emits  $\eta$   $\gamma$  rays per disintegration, the emission rate  $\xi$  of that source is

$$\xi \text{ (}\gamma \text{ rays/sec)} = A \text{ (Bq)} \times 1 \text{ (dps/Bq)} \times \eta \text{ (}\gamma \text{ rays/dis)} \quad (11-1)$$

If the counting rate recorded from this source is  $R$  [counts per second (cps)], then the detection efficiency  $D$  for the measuring system is

$$D = R/\xi \quad (11-2)$$

Alternatively, if the emission rate  $\xi$  and detection efficiency  $D$  are known, one can estimate the counting rate that will be recorded from the source from

$$R = D\xi \quad (11-3)$$

In general, it is desirable to have as large a detection efficiency as possible, so that a maximum counting rate can be obtained from a minimum amount of activity. Detection

efficiency is affected by several factors, including the following:

1. The *geometric efficiency*, which is the efficiency with which the detector intercepts radiation emitted from the source. This is determined mostly by detector size and the distance from the source to the detector.
2. The *intrinsic efficiency* of the detector, which refers to the efficiency with which the detector absorbs incident radiation events and converts them into potentially usable detector output signals. This is primarily a function of detector thickness and composition and of the type and energy of the radiation to be detected.
3. The fraction of output signals produced by the detector that are recorded by the counting system. This is an important factor in *energy-selective counting*, in which a pulse-height analyzer is used to select for counting only those detector output signals within a desired amplitude (energy) range.
4. *Absorption and scatter* of radiation within the source itself, or by material between the source and the radiation detector. This is especially important for in vivo studies, in which the source activity generally is at some depth within the patient.

In theory, one therefore can describe detection efficiency  $D$  as a product of individual factors,

$$D = g \times \varepsilon \times f \times F \quad (11-4)$$

where  $g$  is the geometric efficiency of the detector,  $\varepsilon$  is its intrinsic efficiency,  $f$  is the fraction of output signals from the detector that falls within the pulse-height analyzer window, and  $F$  is a factor for absorption and scatter occurring within the source or between the source and detector. Each of these factors are considered in greater detail in this section. Most of the discussion is related to the detection of  $\gamma$  rays with NaI(Tl) detector systems. Basic equations are presented for somewhat idealized conditions. Complications that arise when the idealized conditions are not met also are discussed. An additional factor applicable for radionuclide imaging instruments is the collimator efficiency, that is, the efficiency with which the collimator transmits radiation to the detector. This is discussed in Chapter 13.

## 2. Geometric Efficiency

Radiation from a radioactive source is emitted *isotropically*, that is, with equal intensity in all directions. At a distance  $r$  from a point source of  $\gamma$ -ray-emitting radioactivity, the emitted radiation passes through the surface of an imaginary sphere having a surface area  $4\pi r^2$ . Thus the flux  $I$  of radiation passing through the sphere per unit of surface area, in units of  $\gamma$  rays/sec/cm<sup>2</sup>, is

$$I = \xi / 4\pi r^2 \quad (11-5)$$

where  $\xi$  is the emission rate of the source and  $r$  is given in centimeters. As distance  $r$  increases, the flux of radiation decreases as  $1/r^2$  (Fig. 11-1). This behavior is known as the *inverse-square law*. It has important implications for detection efficiency as well as for radiation safety considerations (see Chapter 23). The inverse-square law applies to all types of radioactive emissions.

The inverse-square law can be used to obtain a first approximation for the geometric efficiency of a detector. As illustrated in Figure 11-1, a detector with surface area  $A$  placed at a distance  $r$  from a point source of radiation and facing toward the source will intercept a fraction  $A/4\pi r^2$  of the emitted radiation. Thus its geometric efficiency  $g_p$  is

$$g_p \approx A/4\pi r^2 \quad (11-6)$$

where the subscript  $p$  denotes a point source. The approximation sign indicates that the equation is valid only when the distance from the point source to the detector is large in comparison with detector size, as discussed in the following paragraphs.

### EXAMPLE 11-1

Calculate the geometric efficiency for a detector of diameter  $d = 7.5$  cm at a distance  $r = 20$  cm from a point source.

#### Answer

The area,  $A$ , of the detector is

$$A = \pi d^2/4 = \pi[(7.5)^2/4] \text{ cm}^2$$

Therefore, from Equation 11-6,

$$\begin{aligned} g_p &\approx A/4\pi r^2 \\ &\approx \pi (7.5)^2/[4 \times 4\pi (20)^2] \\ &\approx (7.5)^2/[16 \times (20)^2] \\ &\approx 0.0088 \end{aligned}$$

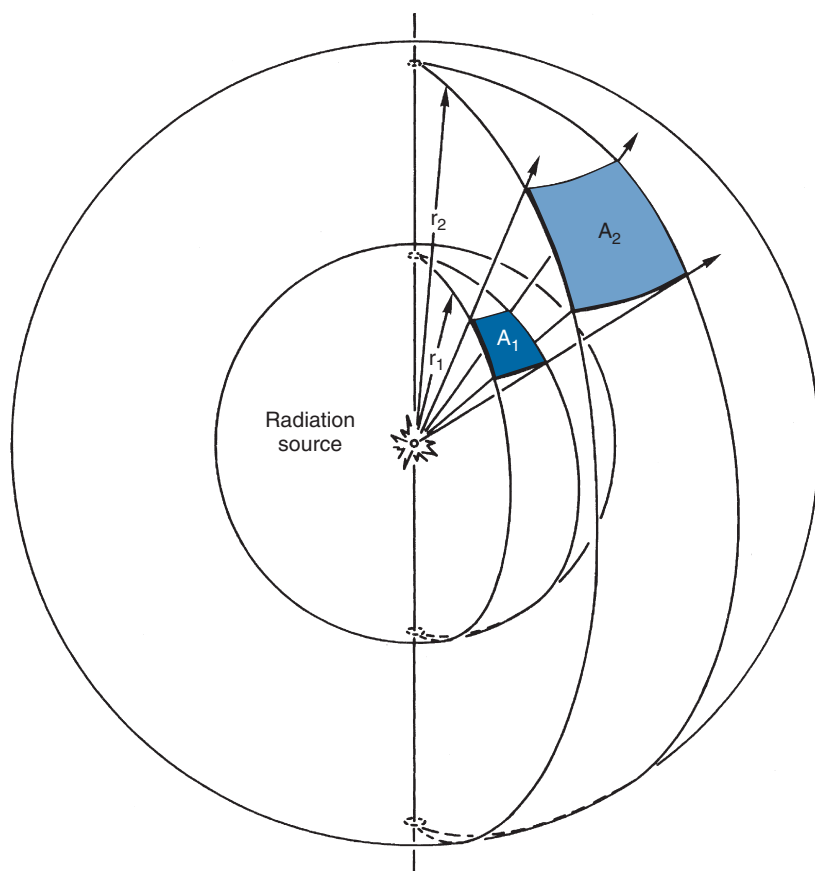


**FIGURE 11-1** Illustration of the inverse-square law. As the distance from the radiation source increases from  $r_1$  to  $r_2$ , the radiations passing through  $A_1$  are spread out over a larger area  $A_2$ . Because  $A \propto r^2$ , the intensity of radiation *per unit area* decreases as  $1/r^2$ .

Thus the detector described in [Example 11-1](#) intercepts less than 1% of the emitted radiation and has a rather small geometric efficiency, in spite of its relatively large diameter. At twice the distance (40 cm), the geometric efficiency is smaller by another factor of 4.

[Equation 11-6](#) becomes inaccurate when the source is “close” to the detector. For example, for a source at  $r = 0$ , it predicts  $g_p = \infty$ . An equation that is more accurate at close distances for point sources located on the central axis of a circular detector is

$$g_p \approx (1/2)(1 - \cos\theta) \quad (11-7)$$

where  $\theta$  is the angle subtended between the center and edge of the detector from the source ([Fig. 11-2](#)). For example, when the radiation source is in contact with the surface of a circular detector,  $\theta = 90$  degrees and  $g_p = 1/2$  ([Fig. 11-3A](#)).

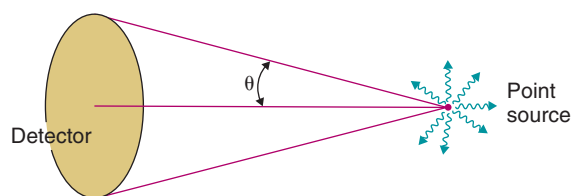


**FIGURE 11-2** Point-source geometric efficiency for a circular large-area detector placed relatively close to the source depends on the angle subtended,  $\theta$  ([Equation 11-7](#)).

Geometric efficiency can be increased by making  $\theta$  even larger. For example, at the bottom of the well in a standard well counter ([Chapter 12, Section A.2](#)) the source is partially surrounded by the detector ([Fig. 11-3B](#)) so that  $\theta \approx 150$  degrees and  $g_p \approx 0.93$ . In a liquid scintillation counter (see [Chapter 12, Section C](#)), the source is immersed in the detector material (scintillator fluid), so that  $\theta = 180$  degrees and  $g_p = 1$  ([Fig. 11-3C](#)).

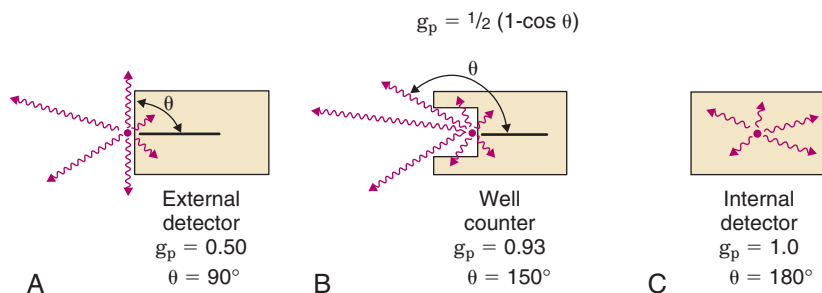


**FIGURE 11-3** Examples of point-source geometric efficiencies computed from Equation 11-7 for different source-detector geometries.

Equation 11-7 avoids the obvious inaccuracies of Equation 11-6 for sources placed close to the detector; however, even Equation 11-7 has limitations when the attenuation by the detector is significantly less than 100%. This problem is discussed further in Section A.5.

The approximations given by Equations 11-6 and 11-7 apply to point sources of radiation located on the central axis of the detector. They also are valid for distributed sources having dimensions that are small in comparison to the source-to-detector distance; however, for larger sources (e.g., source diameter  $\geq 0.3r$ ) more complex forms are required.<sup>1</sup>

### 3. Intrinsic Efficiency

The fraction of radiation striking the detector that interacts with it is called the *intrinsic efficiency*  $\varepsilon$  of the detector:

$$\varepsilon = \frac{\text{no. of radiations interacting with detector}}{\text{no. of radiations striking detector}} \quad (11-8)$$

Intrinsic efficiency ranges between 0 and 1 and depends on the type and energy of the radiation and on the attenuation coefficient and thickness of the detector. For a point source located on the central axis of a  $\gamma$ -ray detector, it is given by

$$\varepsilon = 1 - e^{-\mu_l(E)x} \quad (11-9)$$

where  $\mu_l(E)$  is the linear attenuation coefficient of the detector at the  $\gamma$ -ray energy of interest,  $E$ , and  $x$  is the detector thickness. In Equation 11-9 it is assumed that any interaction of the  $\gamma$  ray in the detector produces a potentially useful signal from the detector, although not necessarily all are recorded if energy-selective counting is used, as described in Section A.4.

The mass attenuation coefficient  $\mu_m$  versus  $E$  for NaI(Tl) is shown in Figure 6-17. Numerical values are tabulated in Appendix D. Values of  $\mu_l$  for Equation 11-9 may be obtained by multiplication of  $\mu_m$  by  $3.67 \text{ g/cm}^3$ , the density of NaI(Tl). Figure 11-4 shows intrinsic efficiency versus  $\gamma$ -ray energy for NaI(Tl) detectors of different thicknesses. For energies below approximately 100 keV, intrinsic efficiency is near unity for NaI(Tl) thicknesses greater than approximately 0.5 cm. For greater energies, crystal thickness effects become significant, but a 5-cm-thick crystal provides  $\varepsilon > 0.8$  over most of the energy range of interest in nuclear medicine.

The intrinsic efficiency of semiconductor detectors also is energy dependent. Because of its low atomic number, silicon (Si,  $Z=14$ ) is used primarily for low-energy  $\gamma$  rays and x rays ( $\leq 100 \text{ keV}$ ), whereas germanium (Ge,  $Z=32$ ) is preferred for higher energies. The effective atomic number of NaI(Tl) is approximately 50 (Table 7-2), which is greater than either Ge or Si; however, comparison with Ge is complicated by the fact that Ge has a greater density than NaI(Tl) ( $\rho = 5.68 \text{ g/cm}^3$  vs.  $3.67 \text{ g/cm}^3$ ). The linear attenuation coefficient of NaI(Tl) is greater than that of Ge for  $E \leq 250 \text{ keV}$ , but at greater energies the opposite is true; however, differences in cost and available physical sizes favor NaI(Tl) over Ge or Si detectors for most applications. The effective atomic numbers of cadmium telluride (CdTe) and cadmium zinc telluride (CZT) detectors are similar to that of NaI(Tl) (see Tables 7-1 and 7-2). They also have higher densities ( $\rho \approx 6 \text{ g/cm}^3$ ). Thus for detectors of similar thickness, these detectors have somewhat greater intrinsic detection efficiencies than NaI(Tl).

Gas-filled detectors generally have reasonably good intrinsic efficiencies ( $\varepsilon \approx 1$ ) for particle radiations ( $\beta$  or  $\alpha$ ) but not for  $\gamma$  and x

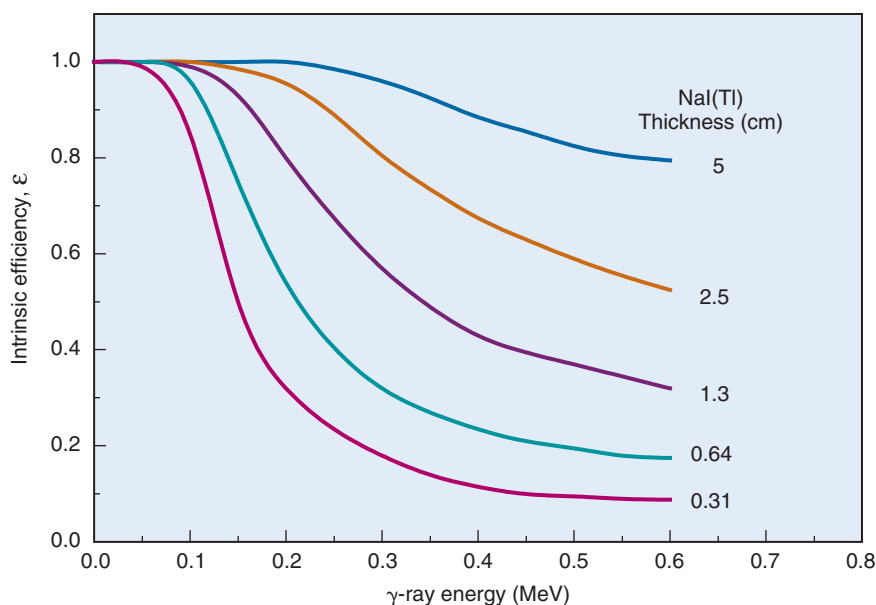


FIGURE 11-4 Intrinsic efficiency versus  $\gamma$ -ray energy for NaI(Tl) detectors of different thicknesses.

rays. Linear attenuation coefficients for most gases are quite small because of their low densities (e.g.,  $\rho \approx 0.0013 \text{ g/cm}^3$  for air). In fact, most gas-filled detectors detect  $\gamma$  rays primarily by the electrons they knock loose from the walls of the detector into the gas volume rather than by direct interaction of  $\gamma$  and x rays with the gas. Intrinsic efficiencies for Geiger-Müller (GM) tubes, proportional counters, and ionization chambers for  $\gamma$  rays are typically 0.01 (1%) or less over most of the nuclear medicine energy range. Some special types of proportional counters, employing xenon gas at high pressures or lead or leaded glass  $\gamma$ -ray converters,\* achieve greater efficiencies, but they still are generally most useful for  $\gamma$ - and x-ray energies below approximately 100 keV.

#### 4. Energy-Selective Counting

The intrinsic efficiency computed from Equation 11-9 for a  $\gamma$ -ray detector assumes that all  $\gamma$  rays that interact with the detector produce an output signal; however, not all output signals are counted if a pulse-height analyzer

is used for energy-selective counting. For example, if counting is restricted to the photopeak, most of the  $\gamma$  rays interacting with the detector by Compton scattering are not counted.

The fraction of detected  $\gamma$  rays that produce output signals within the pulse-height analyzer window is denoted by  $f$ . The fraction within the photopeak is called the *photofraction*  $f_p$ . The photofraction depends on the detector material and on the  $\gamma$ -ray energy, both of which affect the probability of photoelectric absorption by the detector. It depends also on crystal size (see Fig. 10-8) because with a larger-volume detector there is a greater probability of a second interaction to absorb the scattered  $\gamma$  ray following a Compton-scattering interaction in the detector (or of annihilation photons following pair production). Figure 11-5 shows the photofraction versus energy for NaI(Tl) detectors of different sizes.

If energy-selective counting is not used, then  $f \approx 1$  is obtained. (Generally, some energy discrimination is used to reject very small amplitude noise pulses.) Full-spectrum counting provides the maximum possible counting rate and is used to advantage when a single radionuclide is counted, with little or no interference from scattered radiation. This applies, for example, to many in vitro measurements (see Chapter 12).

\*A converter is a thin layer of material with relatively good  $\gamma$ -ray stopping power that is placed in front of or around the sensitive volume of a gas-filled detector. Recoil electrons ejected from  $\gamma$ -ray interactions in the converter are detected within the sensitive volume of the detector.

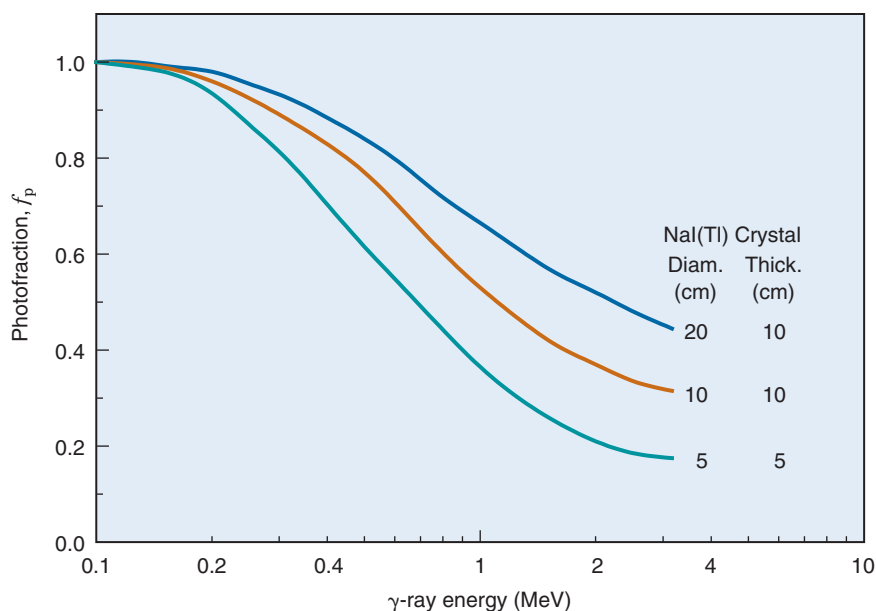


**FIGURE 11-5** Photofraction versus  $\gamma$ -ray energy for cylindrical NaI(Tl) detectors of different sizes.

## 5. Some Complicating Factors

### a. Nonuniform Detection Efficiency

Equations 11-6, 11-7, and 11-9 are somewhat idealized in that they assume that radiation is detected with uniform efficiency across the entire surface of the detector. In some cases, this assumption may be invalid. Figure 11-6 shows some examples for different trajectories from a point source of radiation. For trajectory A, the thickness of detector encountered by the radiation and employed for the calculation of intrinsic efficiency in Equation 11-9 conforms to what normally would be defined as the “detector thickness” in that equation. However, for trajectory B, a greater thickness is encountered and the intrinsic efficiency is larger. On the other hand, for trajectory C, near the edge of the detector, a smaller thickness of detector material is encountered and the intrinsic efficiency is smaller. Partial penetration of the beam for trajectory C sometimes is called an *edge effect*.

Thus, unless the attenuation by the detector is “very high” (essentially 100% within a thin layer near the surface), the intrinsic efficiency will vary across the surface of the detector. As well, the detector diameter (or area) used for the calculation of geometric efficiency in Equation 11-6 or 11-7 becomes ill-defined when edge effects are significant. When the complications illustrated in Figure 11-6 are significant, detection efficiency must be calculated by methods of integral calculus,

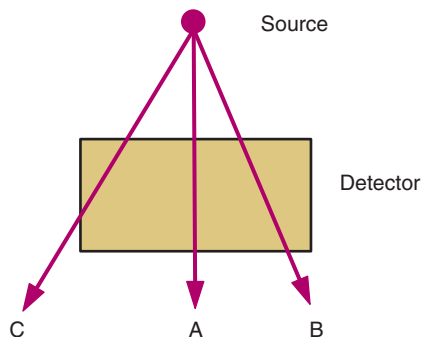


**FIGURE 11-6** Three possible trajectories for radiations striking a detector from a point source, each having a different intrinsic detection efficiency.

rather than with the simplified equations described thus far. The calculations are complex and a complete analysis is beyond the scope of this text, but they have been analyzed in other books.<sup>2</sup> A few practical implications derived from more advanced calculations are presented here.

The nonuniform attenuation illustrated in Figure 11-6 affects both geometric efficiency (edge effects) and intrinsic efficiency. The parameter that accounts for both of these quantities is the *total detection efficiency*,  $\epsilon_t$ . When idealized conditions apply, this can be obtained simply by multiplying the result of Equation 11-6 or 11-7 by the result from Equation 11-9



$$\varepsilon_t = g_p \times \varepsilon \quad (11-10)$$

It is reasonable to use Equation 11-10 to compute total detection efficiency if the resulting discrepancy from a more exact calculation is “small,” for example, less than 10%. If the discrepancy is larger, then one must consider using the more complex methods of integral calculus.

Figure 11-7 shows three detector profiles with different levels of effect for the trajectories shown in Figure 11-6. As compared with a “box” profile (i.e., one with equal thickness and width), a “wide” profile presents a greater range of potential detector thicknesses (trajectory B in Fig. 11-6), whereas a “narrow” profile has a greater fraction of its area affected by edge effects (trajectory C in Fig. 11-6). In addition to the profile of the detector, the extent of these effects depends on the attenuation properties of the detector (material and thickness) and on the source-to-detector distance. Thus one cannot provide a “one-size-fits-all”

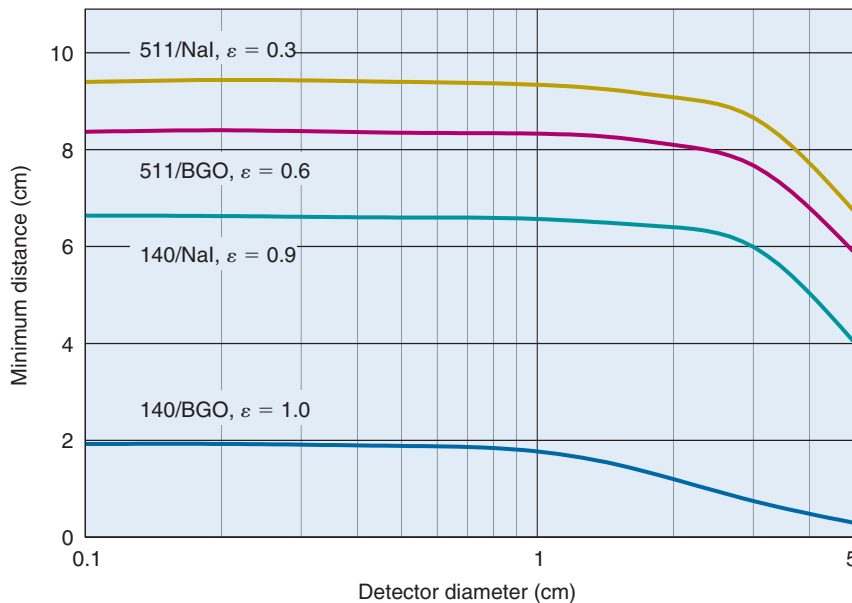
rule of thumb for when it is necessary to use the more advanced equations instead of the simplified equations presented earlier. All of these parameters must be considered for making this determination.

Figure 11-8 presents a graph that can be helpful for this purpose. It applies to 1-cm-thick  $\gamma$ -ray detectors for two photon energies (140 keV and 511 keV) and two detector materials [NaI(Tl) and bismuth germanate (BGO)] that are used in nuclear medicine. In this graph, a “narrow” detector would lie toward the left end of the horizontal axis, and a “wide” one would lie toward the right. A “box” detector would have a diameter of 1 cm.

Also indicated on the graph are the intrinsic efficiencies, computed from Equation 11-9 for the central ray A in Figure 11-6, for different combinations of these photon energies and detectors. The curves indicate the minimum source-to-detector distance versus detector diameter at which the total detection



**FIGURE 11-7** Examples of detector profiles with different complications for the computation of total detection efficiency.



**FIGURE 11-8** Minimum distance at which simplified equations for detection efficiency (Equations 11-7, 11-9, and 11-10) can be used with errors of less than 10% for 1-cm-thick detectors of different diameters and different combinations of photon energy-detector material. The graph assumes a point source of radiation is placed on the central axis of the detector. Photon energies are measured in keV. At closer distances, total detection efficiency must be computed from more-complicated mathematical models (see reference 2).

efficiency computed using Equations 11-7 and 11-9 in Equation 11-10 is accurate to within 10%. At distances closer than the minimum distance, the simplified calculations are inaccurate by more than 10%, and the more complicated methods of integral calculus should be used to compute the total detection efficiency,  $\epsilon_t$ .<sup>2</sup>

Figure 11-8 shows that for detectors having a high value of intrinsic efficiency (e.g., BGO detector for 140-keV photons,  $\epsilon \approx 1$ ), the simplified equations can be used with less than 10% error at relatively close distances. Even for the “narrow” detector profile shown in Figure 11-7, they can be used within 2 cm of the detector. At the other extreme, for a detector having a low value of intrinsic efficiency [e.g., NaI(Tl) for 511-keV positron annihilation photons,  $\epsilon \approx 0.3$ ], the simplified equations fail within approximately 10 cm from a “narrow” detector and within about 5 cm from a “wide” one.

Figure 11-8 provides general guidance as to when the simplified equations can be used for estimating relative detection efficiencies on existing systems in a laboratory or for preliminary design work for a new detector system. It also can be used for guidance with other combinations of photon energy and detector material having dimensions and values of  $\epsilon$  similar to those indicated on the graph. For more precise design work, it generally is preferable to go directly to the methods of integral calculus. Alternatively, Monte Carlo techniques, using a computer to simulate photon trajectories and interactions for a large number of individual photons originating from a radioactive source, can be used to estimate detection efficiency.

## b. Detection of Simultaneously Emitted Radiations in Coincidence

Yet another complicating factor is that some radionuclides emit multiple  $\gamma$  rays in cascaded fashion from a single nuclear disintegration. In Figure 3-3, for example,  $\beta_1$  may be followed by the emission of multiple  $\gamma$  rays (e.g.,  $\gamma_5$  and  $\gamma_2$ ). In this example and in most other cases of cascaded  $\gamma$  emissions, the  $\gamma$  rays are emitted within a few nanoseconds of each other, which is well within the resolving time of most detectors (see Section C). If the two  $\gamma$  rays are detected simultaneously (*coincidence detection*), they are recorded as a single event having an apparent energy equal to the sum of the energies deposited in the detector by the individual  $\gamma$  rays. If energy-selective

counting is used, such as with the photopeak of one or the other  $\gamma$  ray, the pulse from the resulting event could be moved out of the selected analyzer window, thereby decreasing the counting rate for that  $\gamma$  ray (see Fig. 10-7). Note, however, that simultaneous detection does not occur when there is a significant delay before the emission of the second  $\gamma$  ray, such as in metastable states (see Chapter 3, Section E).

A full treatment of the problem of coincidence detection of cascaded emissions is beyond the scope of this text. However, the following discussion provides a first-level analysis and an indication of when it must be taken into consideration. Suppose that two  $\gamma$  rays, which we denote as  $\gamma_1$  and  $\gamma_2$ , are emitted simultaneously, in cascaded fashion, with relative frequencies per disintegration  $\eta_1$  and  $\eta_2$ . (Note that it is not necessary that  $\eta_1 = \eta_2$ ; e.g.,  $\eta_2$  could be reduced by alternative decay pathways that result in nondetectable emissions, such as internal conversion.) Suppose further that the total (full-spectrum) detection efficiencies for the two  $\gamma$  rays are  $D_1$  and  $D_2$ , respectively. The probability that a single nuclear disintegration will result in the detection of  $\gamma_1$  is

$$p_1 = \eta_1 D_1 \quad (11-11)$$

In the absence of coincidence detection, the counting rate recorded for  $\gamma_1$  would be

$$R_1 = p_1 \times A \quad (11-12)$$

where  $A$  is the source activity in Bq. Similarly, in the absence of coincidence detection, the counting rate resulting from detection of  $\gamma_2$  events would be

$$R_2 = p_2 \times A \quad (11-13)$$

Thus, if one did not account for the possibility of coincidence detection, the predicted full-spectrum counting rate for the source would be  $(R_1 + R_2)$ .

Taking into account the possibility of coincidence detection, the probability that  $\gamma_1$  and  $\gamma_2$  will be detected simultaneously is

$$p_{12} = \eta_1 D_1 \times \eta_2 D_2 \quad (11-14)$$

and the counting rate for simultaneously detected events is

$$R_{12} = p_{12} \times A \quad (11-15)$$



With full-spectrum counting, each coincidence event removes one event each from  $R_1$  and  $R_2$ , replacing it with an event in  $R_{12}$ . Thus the recorded full-spectrum counting rate would be  $(R_1 + R_2 - R_{12})$ .

A similar analysis can be performed for photopeak counting. In this case, the total-spectrum detection efficiency is replaced by the photopeak detection efficiency for each  $\gamma$  ray. The counting rate in each photopeak is reduced by  $R_{12}$ ; that is, they would be  $(R_1 - R_{12})$  and  $(R_2 - R_{12})$ , and the summation photopeak counting rate would be  $R_{12}$ .

In actual practice, calculating the effect of detecting simultaneously emitted photons on recorded counting rates is somewhat more complicated than indicated by the previous equations. For example, for calculating the effect on photopeak counting rates, one should take into account the possibility of simultaneous detection of events in the Compton portion of the spectrum, which also could “move” events out of the photopeak, or possibly add up to create apparent photopeak events. A more detailed analysis also would include the possibility of angular correlations between the directions in which the two  $\gamma$  rays are emitted. In many cases, this would lead to different values of detection efficiencies for the two  $\gamma$  rays.

Nevertheless, the first-level analysis provided in the preceding discussion can give an indication of when the effects of coincidence detection can be significant. For example, from Equations 11-14 and 11-15, it can be seen that the effects depend on the values of  $\eta_1$  and  $\eta_2$  and on detection efficiencies  $D_1$  and  $D_2$ . Thus if the primary emission of interest is  $\gamma_1$ , and,  $\eta_1 \gg \eta_2$ , the effect of  $\gamma_2$  on  $R_1$  (or  $R_1 + R_2$ ) would be relatively small. As well, the effects are most severe in counting systems having high values of detection efficiency.

An example is the well counter, which generally has a high total detection efficiency. This is illustrated by Figure 10-7, showing how the coincidence sum peak for the two  $\gamma$  rays of  $^{111}\text{In}$  increases dramatically when the source is moved from a location outside the well-counter detector where detection efficiency is low to a location inside it where it is high. When questions arise, the first-level analysis presented above can be used to estimate the relative magnitude of the effects of coincidence counting of cascaded  $\gamma$  rays. Experimental data can further help to resolve the issue, for example, by comparing the spectra with the source at different locations, as in Figure 10-7.

### c. Attenuation and Scatter of Radiation Outside the Detector

A final complication that we consider is the possibility of absorption and scatter of radiation before it reaches the detector. The analysis to this point assumes that radiation passes unobstructed, without absorption or scattering, from the source to the detector (e.g., as in Fig. 11-1). However, when the radiation source is embedded at depth within an absorbing and scattering medium, as it is for most in vivo measurements, the calculation of detection efficiency is complicated by attenuation and scattering effects.

Absorption generally causes a decrease in the recorded counting rate, but scattered radiation may lead to a decrease or an increase, depending on whether there is more scattering away from or toward the detector. For example, the counting rate for a source at a shallow depth in a scattering medium actually may be greater than for the same source in air because the added contribution from backscattering may more than compensate for a small reduction in counting rate by absorption. (See also the discussion of the buildup factor in Chapter 6, Section D.3). At greater depths absorption effects may predominate.

Corrections for attenuation and scattering for in vivo measurements are complicated because they depend on several factors, including the  $\gamma$ -ray energy, depth of the source in the absorbing and scattering medium, use of energy-selective counting, and so forth. Figure 11-9 shows the general effects versus  $\gamma$ -ray energy for a point source 7.5-cm deep in tissue-equivalent material and a NaI(Tl) counting system. The fraction of  $\gamma$  rays emitted from the source that are *neither scattered nor absorbed* on their way to the detector increases with  $\gamma$ -ray energy because absorption and scattering coefficients decrease with increasing energy. The fraction of  $\gamma$  rays *absorbed* in the tissue-equivalent material decreases with energy to a negligible fraction above approximately 100 keV.

Figure 11-9 also shows that the fraction of  $\gamma$  rays *scattered* at first increases with  $\gamma$ -ray energy because absorption effects decrease, leaving more  $\gamma$  rays to be scattered. This fraction reaches a maximum at approximately 100 keV, after which it also decreases with increasing energy. If energy-selective counting is used, the fraction of Compton-scattered  $\gamma$  rays recorded in the photopeak decreases with increasing  $\gamma$ -ray energy. This reflects the

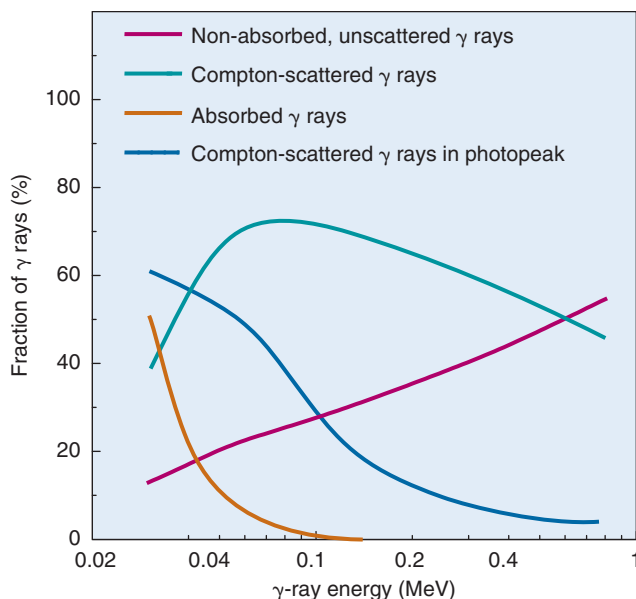


**FIGURE 11-9** General effects of  $\gamma$ -ray energy on the fraction of  $\gamma$  rays scattered or absorbed from a point source 7.5 cm deep in tissue and on the fraction of unscattered  $\gamma$  rays and scattered  $\gamma$  rays having sufficient energy to be recorded with a photopeak window and NaI(Tl) detector. (From Anger HO: *Radioisotope cameras*. In Hine GJ, editor: *Instrumentation in Nuclear Medicine, Vol 1*. New York, 1967, Academic Press, p 514.)

increasing energy separation between scattered  $\gamma$  rays and the photopeak (see Fig. 10-10). With semiconductor detectors (Ge, Si, CdTe, or CZT), this fraction is much smaller because of their ability to clearly resolve scattered  $\gamma$  rays from the photopeak (see Figs. 10-14 and 10-15).

Another factor affecting detection efficiency is attenuation by the housing material of the detector. Most  $\gamma$ -ray detectors are fabricated with relatively thin entrance windows, such as thin layers of aluminum, so that their attenuation is negligible. Detectors designed for applications involving very-low-energy  $\gamma$  rays sometimes are constructed with ultra-thin (and fragile) entrance windows of alternative materials, such as beryllium. However, attenuation can become significant if the detector is used outside the range of its intended applications. Information provided by the manufacturer can be used to estimate this effect in questionable situations.

Attenuation by the detector housing can be severe in  $\beta$ -particle counting. This is discussed separately in Section B.

## 6. Calibration Sources

Detection efficiencies can be determined experimentally using *calibration sources*. A calibration source is one for which the activity or emission rate is known accurately. This

determination usually is made by the commercial supplier of the source.

Detection efficiency can be determined by measuring the counting rate recorded from the calibration source and applying Equation 11-2. This method generally is satisfactory for systems in which a standard measuring configuration is used and for which the calibration source accurately simulates the shape and distribution of the sources usually measured with the system. For example, “rod standards” (Fig. 11-10) are used for determining detection efficiencies of well counters for test-tube samples.

Some  $\gamma$ -ray-emitting source materials that are available as calibration standards are listed in Table 11-1. Most are quite long-lived. Detection efficiencies for short-lived radionuclides can be estimated from measurements made on a calibration standard having similar emission characteristics. For example,  $^{57}\text{Co}$  ( $E_\gamma = 122 \text{ keV}$  and  $136 \text{ keV}$ ) frequently is used to simulate  $^{99\text{m}}\text{Tc}$  ( $E_\gamma = 140 \text{ keV}$ ). (Cobalt-57 is sometimes called “mock  $^{99\text{m}}\text{Tc}$ .”) For most detection systems, intrinsic efficiencies at these three energies are virtually identical. Therefore the detection efficiency per emitted  $\gamma$  ray as calculated from Equation 11-2 would be the same for  $^{99\text{m}}\text{Tc}$  and  $^{57}\text{Co}$  (assuming the same energy-selective counting conditions were used, e.g., photopeak counting for both).

**FIGURE 11-10** “Rod standards” containing accurately known quantities of different radionuclides used for determining the detection efficiencies of well counters. The sources are meant to simulate radioactivity in test tubes.

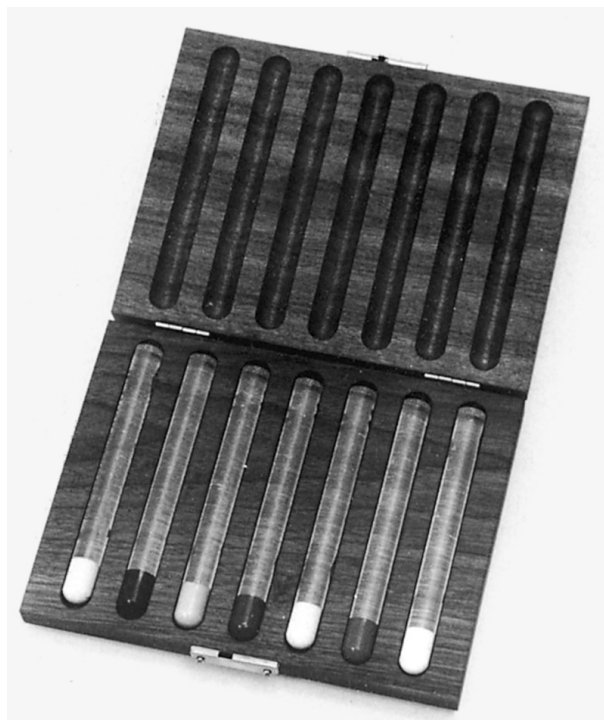


**TABLE 11-1**  
**PROPERTIES OF SOME  $\gamma$ -RAY SOURCES USED AS CALIBRATION STANDARDS**

Radionuclide	Half-Life	$\gamma$ -Ray or x-Ray Energy (keV) *	Emission Frequency ( $\gamma$ or x rays/dis)
$^{22}\text{Na}$	2.60 yr	511	1.798
		1274	0.999
$^{54}\text{Mn}$	312 d	834.8	1.000
$^{57}\text{Co}$	272 d	14.4	0.095
		122.1	0.856
		136.5	0.105
$^{60}\text{Co}$	5.27 yr	1173	0.999
		1333	1.000
$^{68}\text{Ge}$	271 d	511	1.780
$^{85}\text{Sr}$	64.9 d	514	0.980
$^{109}\text{Cd}$	463 d	22.0 ( $K_{\alpha}$ x ray)	0.842
		24.9 ( $K_{\beta}$ x ray)	0.178
		88.0	0.037
$^{113}\text{Sn}$	115 d	24.1 ( $K_{\alpha}$ x ray)	0.794
		27.3 ( $K_{\beta}$ x ray)	0.172
		391.7	0.649
$^{129}\text{I}$	$15.7 \times 10^6$ yr	29.7 ( $K_{\alpha}$ x ray)	0.571
		33.6 ( $K_{\beta}$ x ray)	0.132
		39.6	0.075
$^{137}\text{Cs}$	30 yr	32.0 ( $K_{\alpha}$ x ray)	0.057
		36.4 ( $K_{\beta}$ x ray)	0.013
		661.7	0.851

Data adapted from NCRP Report No. 58: *A Handbook of Radioactivity Measurements Procedures*, ed 2, Bethesda, MD, 1985, National Council on Radiation protection and Measurements.

\*Only predominant photon emissions are listed.

If the detection efficiency is determined on the basis of cps/Bq, one must take into account the differing emission frequencies of the two radionuclides. Cobalt-57 emits 0.96  $\gamma$ /dis ( $\gamma$  rays per disintegration), whereas  $^{99m}\text{Tc}$  emits 0.89  $\gamma$ /dis (see Appendix C). Therefore the counting rate per Bq of  $^{99m}\text{Tc}$  would be a factor of  $0.89/0.96 = 0.93$  smaller than that measured per Bq of  $^{57}\text{Co}$ . This should be applied as a correction factor to the counting rate per Bq determined for  $^{57}\text{Co}$  to obtain the counting rate per Bq for  $^{99m}\text{Tc}$ .

Calibration sources also are used in phantoms simulating the human anatomy for estimating the detection efficiency for in vivo measurement systems; however, the result is only as accurate as the phantom and source distribution are accurate for simulating the human subject. For example, a 1-cm discrepancy between source depths in the phantom and in the human subject may result in a 10% to 20% difference in counting rate (see Chapter 12, Section F.1).

## B. PROBLEMS IN THE DETECTION AND MEASUREMENT OF $\beta$ PARTICLES

Because of their relatively short ranges in solid materials,  $\beta$  particles create special detection and measurement problems. These

problems are especially severe with low-energy  $\beta$ -particle emitters, such as  $^3\text{H}$  and  $^{14}\text{C}$ . The preferred method for assay of these radionuclides is by liquid scintillation counting techniques (Chapters 7 and 12); however, these techniques are not applicable in all situations, such as when surveying a bench top with a survey meter to detect  $^{14}\text{C}$  contamination (Chapter 23). A complete discussion of the problems arising in detection and assay of  $\beta$ -particle emitters is beyond the scope of this book; however, a few of the practical problems are described briefly.

A survey meter can be used to detect surface contamination by  $\beta$ -particle emitters provided it has an entrance window sufficiently thin to permit the  $\beta$  particles to enter the sensitive volume of the detector. Figure 11-11 shows relative counting rate versus entrance window thickness for two  $\beta$ -emitting radionuclides. Efficient detection of low-energy  $\beta$  emitters requires a very thin entrance window, preferably fabricated from a low-density material. A typical entrance window for a survey meter designed for  $^3\text{H}$  and  $^{14}\text{C}$  detection is 0.03-mm-thick Mylar ( $\sim 1.3 \text{ mg/cm}^2$  thick).\* Mica and beryllium also

\*Thicknesses of detector windows often are specified in units of mass/area, for example,  $\text{mg/cm}^2$ . To obtain the window thickness, divide by the material density using the same units (e.g.,  $\text{mg/cm}^3$ ).

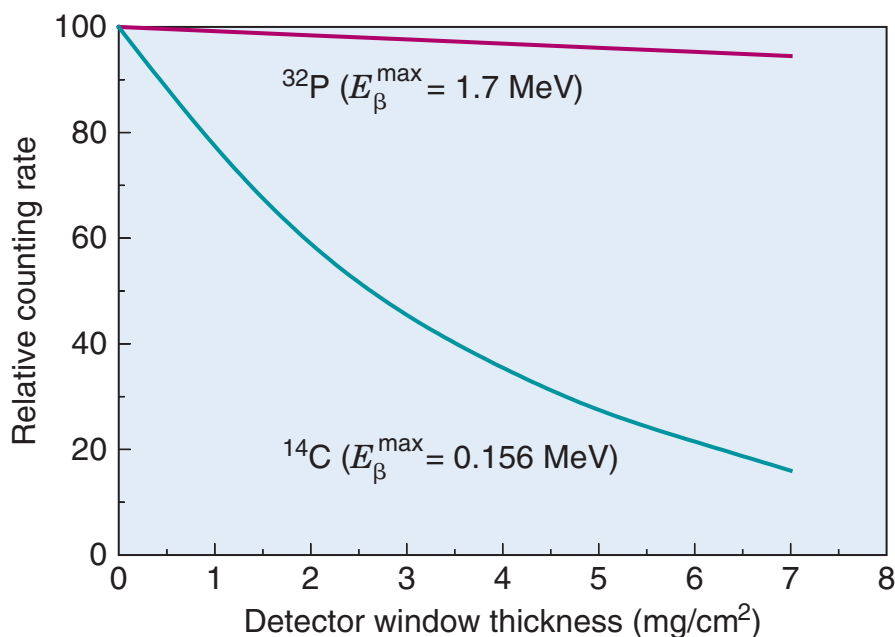


**FIGURE 11-11** Relative counting rate versus detector window thickness for some  $\beta$ -emitting radionuclides. (Adapted from Quimby EH, Feitelberg S, Gross W: *Radioactive Nuclides in Medicine and Biology*. Philadelphia, 1970, Lea & Febiger.)

are used. Such thin windows are very fragile, and usually they are protected by an overlying wire screen. Beta particles that are more energetic (e.g., from  $^{32}\text{P}$ ) can be detected with much thicker and more rugged entrance windows; for example, 0.2-mm-thick aluminum ( $\sim 50 \text{ mg/cm}^2$ ) provides approximately 50% detection efficiency for  $^{32}\text{P}$ .

GM and proportional counters sometimes are used to assay the activities of  $\beta$ -emitting radionuclides in small trays (“planchets”) or similar sample holders. Two serious problems arising in these measurements are *self-absorption* and *backscattering*, as illustrated in Figure 11-12. Self-absorption depends on the sample thickness and the  $\beta$ -particle energy. Figure 11-13 shows relative counting rate versus sample thickness for two  $\beta$  emitters. For  $^{14}\text{C}$  and similar low-energy  $\beta$  emitters, self-absorption in a sample thickness of only a few  $\text{mg/cm}^2$  is sufficient to cause a significant reduction of counting rate. (Note that for water,  $\rho = 1 \text{ g/cm}^3$ ; thus  $1 \text{ mg/cm}^2$  is 0.001-cm thick.) Backscattering of  $\beta$  particles from the sample and sample holder tends to increase the sample counting rate and can amount to 20% to 30% of the total sample counting rate in some circumstances.

Accurate assay of  $\beta$ -emitting radioactive samples by external particle-counting techniques requires careful attention to sample preparation. If only relative counting rates

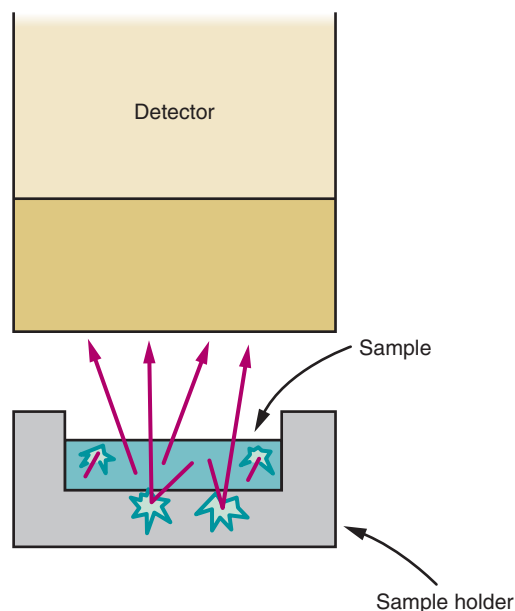


**FIGURE 11-12** Self-absorption and backscattering in  $\beta$ -particle counting.

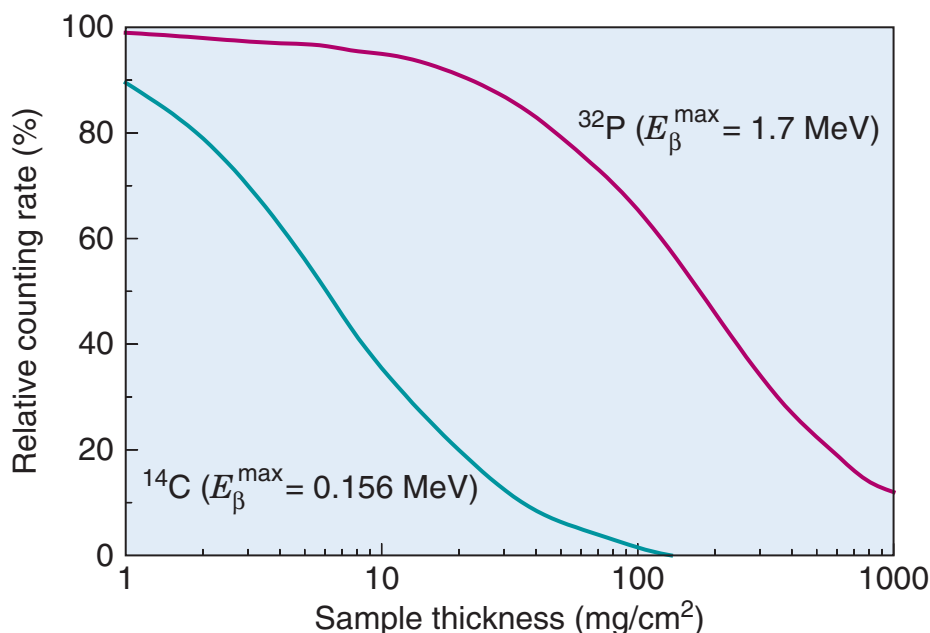


**FIGURE 11-13** Effect of sample self-absorption on counting rate for two  $\beta$  emitters. (Adapted from Quimby EH, Feitelberg S, Gross W: Radioactive Nuclides in Medicine and Biology. Philadelphia, 1970, Lea & Febiger.)



are important, then it is necessary to have sample volumes and sample holders as nearly identical as possible. Other techniques for dealing with these difficult problems are discussed in reference 3.

*Bremsstrahlung counting* can be employed as an indirect method for detecting  $\beta$  particles using detectors that normally are sensitive only to more penetrating radiations such as x rays and  $\gamma$  rays, for example a NaI(Tl) well counter (Chapter 12). Bremsstrahlung counting also was employed in some early studies using  $^{32}\text{P}$  for the detection of brain tumors and still is used occasionally to map the distribution of  $^{32}\text{P}$ -labeled materials administered for therapeutic purposes. Bremsstrahlung counting is effective only for relatively energetic  $\beta$  particles (e.g.,  $^{32}\text{P}$ ,  $E_{\beta}^{\max} = 1.7$  MeV, but not  $^{14}\text{C}$ ,  $E_{\beta}^{\max} = 0.156$  MeV) and requires perhaps 1000 times greater activity than a  $\gamma$ -ray emitter because of the very low efficiency of bremsstrahlung production.

## C. DEAD TIME

### 1. Causes of Dead Time

Every radiation counting system exhibits a characteristic *dead time* or *pulse resolving time*  $\tau$  that is related to the time required to process individual detected events. The pulses produced by a radiation detector have a finite time duration, such that if a second pulse occurs before the first has disappeared, the two pulses will overlap to form a single distorted pulse. With GM detectors, the overlap may occur in the detector itself, during the time that the “avalanche charge” is being collected from a previous pulse, so that the second pulse does not produce a detectable output signal and is lost (see Chapter 7, Section A.4).

With energy-sensitive detectors (scintillation, semiconductor, proportional counter), the overlap usually occurs in the pulse amplifier, causing baseline shift and pulse pile-up (see Chapter 8, Section B.3). Shifted or overlapped pulse amplitudes may fall outside the selected analyzer window, again resulting in a loss of valid events. Such losses are called *dead time losses*. The shorter the dead time, the smaller the dead time losses. The dead time for a GM tube is typically 50–200  $\mu\text{sec}$ . Sodium iodide and semiconductor detector systems typically have dead times in the range of 0.5–5  $\mu\text{sec}$ . Gas proportional counters and

liquid scintillation systems have dead times of 0.1–1  $\mu\text{sec}$ .

Dead time losses also occur in pulse-height analyzers, scalars, computer interfaces, and other components that process pulse signals. Generally scalars and single-channel analyzers have dead times of much less than 1  $\mu\text{sec}$ , whereas multichannel analyzer and computer interface dead times are on the order of a few microseconds. Usually the dead time is given for the counting system as whole; however, if one of the components has a dead time that is long in comparison to the other components, then system dead time is determined by that component.

### 2. Mathematical Models

Counting systems usually are classified as being of the paralyzable or nonparalyzable type. A *nonparalyzable system* is one for which, if an event occurs during the dead time  $\tau$  of a preceding event, then the second event is simply ignored, with no effect on subsequently occurring events (Fig. 11-14). Digital counters, pulse-height analyzers, and computer interfaces frequently behave as nonparalyzable systems. A *paralyzable system* is one for which each event introduces a dead time  $\tau$  whether or not that event actually is counted. Thus an event occurring during the dead time of a preceding event would not be counted but still would introduce its own dead time during which subsequent events could not be recorded. A paralyzable system may be thought of as one with an “extendable” dead time. Most radiation detectors behave as paralyzable systems.

Because of dead time losses, the *observed* counting rate  $R_o$  (cps) is less than the *true*

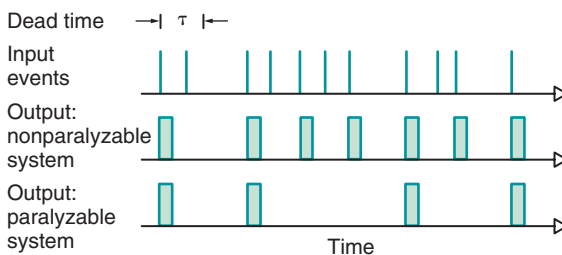


**FIGURE 11-14** Difference in output signals between nonparalyzable and paralyzable systems. Both have dead time  $\tau$  indicated in top line. Second line illustrates randomly occurring input events. With a nonparalyzable system (third line), events are lost if they occur within a time  $\tau$  of a preceding recorded event, whereas with a paralyzable system (fourth line) events are lost if they occur within a time  $\tau$  of any preceding event, regardless of whether that event has been recorded.



counting rate  $R_t$  (cps), where the latter is the counting rate that would be recorded if  $\tau = 0$ . The relationship among  $R_o$ ,  $R_t$ , and  $\tau$  depends on the type of dead time. For nonparalyzable systems,

$$R_o = R_t / (1 + R_t \tau) \quad (11-16)$$

$$R_t = R_o / (1 - R_o \tau) \quad (11-17)$$

where  $\tau$  is given in seconds. If the system has a paralyzable dead time, then

$$R_o = R_t e^{-R_t \tau} \quad (11-18)$$

There is no analytic equation for  $R_t$  as a function of  $R_o$  for the paralyzable case.

Figure 11-15 shows  $R_o$  versus  $R_t$  for the two types of systems. For a nonparalyzable system, the observed counting rate increases asymptotically toward a maximum value

$$R_o^{\max} = 1/\tau \quad (11-19)$$

At very high true counting rates, greater than one count per dead time interval, the system simply records one event per dead time interval, ignoring all the others that occur during the dead time interval between counted events.

For a paralyzable system, the observed counting rate rises to a maximum value given by

$$R_o^{\max} = 1/e\tau \quad (11-20)$$

where  $e$  ( $= 2.718 \dots$ ) is the base of natural logarithms. Then the observed counting rate actually *decreases* with a further increase in true counting rate. This is because additional events serve only to extend the already long dead time intervals without contributing to additional events in the observed counting rate. At very high true counting rates, the observed counting rate actually approaches zero. This is called *counter paralysis*.

Dead time losses are given by the difference between observed and true counting rates,  $R_t - R_o$ , and *percentage losses* are given by

$$\text{percentage losses} = [(R_t - R_o) / R_t] \times 100\% \quad (11-21)$$

When the product  $R_t \tau$  is “small” ( $\leq 0.1$ ), the percentage losses are “small” (i.e.,  $\leq 10\%$ ), and they can be described by the same equation for both paralyzable and nonparalyzable systems

$$\text{percentage losses} \approx (R_t \tau) \times 100\% \quad (11-22)$$

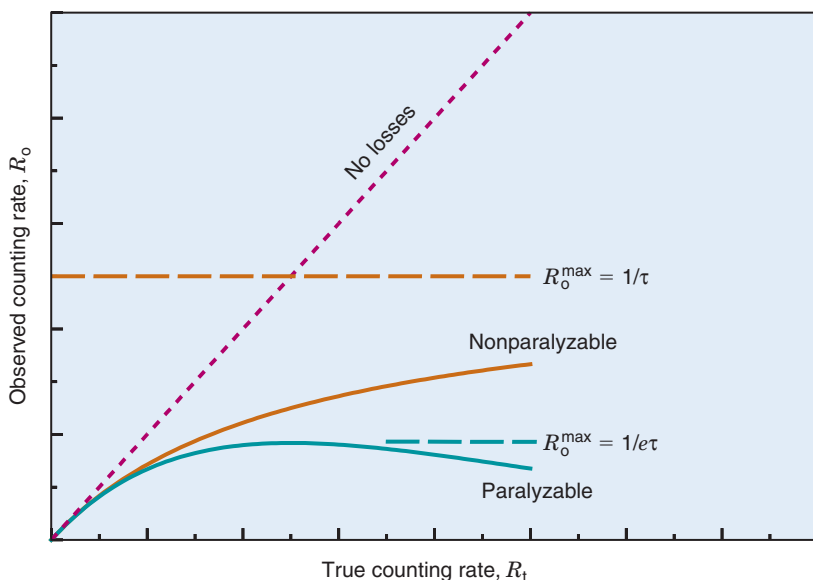


**FIGURE 11-15** Observed ( $R_o$ ) versus true ( $R_t$ ) counting rate curves for paralyzable and nonparalyzable systems having the same dead time value,  $\tau$ .

**EXAMPLE 11-2**

Calculate the percentage losses for a counting system having a dead time of 10  $\mu\text{sec}$  at true counting rates of 10,000 and 100,000 cps.

**Answer**

At 10,000 cps,  $R_t\tau = 10^4 \text{ cps} \times 10^{-5} \text{ sec} = 0.1$ . Because the losses are “small,” Equation 11-22 can be used:

$$\begin{aligned}\text{percentage losses} &\approx (0.1) \times 100\% \\ &\approx 10\%\end{aligned}$$

The observed counting rate would therefore be approximately 9000 cps, that is, 10% less than the true counting rate of 10,000 cps. At 100,000 cps,  $R_t\tau = 10^5 \text{ cps} \times 10^{-5} \text{ sec} = 1.0$ ; thus the losses are not “small.” For a nonparalyzable system, the observed counting rate would be (Equation 11-16)

$$\begin{aligned}R_o &= 100,000 / (1 + 1.0) \text{ cps} \\ &= 50,000 \text{ cps}\end{aligned}$$

that is, the losses would be 50%. For a paralyzable system (Equation 11-18)

$$\begin{aligned}R_o &= 10^5 \times e^{-1.0} \text{ cps} \\ &= 100,000 \times 0.368 \text{ cps} \\ &= 36,800 \text{ cps}\end{aligned}$$

The losses are therefore 100,000 – 36,800 cps = 63,200 cps, or 63.2% (of 100,000 cps).

Example 11-2 illustrates that for a given dead time and true counting rate, the dead time losses for a paralyzable system are greater than those of a nonparalyzable system. This is shown also by Figure 11-15.

Many nuclear medicine systems have multiple components in cascade, each with its own individual dead time. In some cases, one component of a cascaded system may be paralyzable (e.g., the scintillation detector) whereas the other may be nonparalyzable (e.g., a multichannel analyzer interface). In most cases, one component dominates the system and its behavior adequately describes the system behavior. However, if cascaded paralyzable and nonparalyzable components have similar dead times, both components contribute to dead time losses and the behavior is a hybrid of the two. The analysis of such systems is beyond the scope of this text; see references 4 and 5 for further details.

**3. Window Fraction Effects**

With NaI(Tl) and other detectors used for energy-selective counting, any detected event can cause pile-up with any other event in the pulse-height spectrum. Thus if a pulse-height analyzer is used, the number of events lost depends on the *total-spectrum counting rate*, not just on the counting rate within the selected analyzer window. With such systems, the apparent dead time may appear to change with pulse-height analyzer window setting. For example, if a certain fraction of detected events are lost with a given window setting, the same *fraction* will be lost when the analyzer window is narrowed, making it appear that the dead time *per event in the analyzer window* is longer when the narrower window is used.

An approximate equation for apparent dead time is<sup>6</sup>

$$\tau_a = \tau / w_f \quad (11-23)$$

where  $\tau$  is the actual dead time per detected event and  $w_f$  is the *window fraction*, that is, the fraction of detected events occurring within the selected analyzer window. For example, if a NaI(Tl) detector system has a dead time of 1  $\mu\text{sec}$  (amplifier pulse duration) but a narrow window is used so that only 25% of detected events are within the window ( $w_f = 0.25$ ), the apparent dead time will be  $(1/0.25) = 4 \mu\text{sec}$ . Window fractions also change with the amount of scattered radiation recorded by the detector because this also changes the energy spectrum of events recorded by the detector. In general, increased amounts of scattered radiation decrease the window fraction recorded with a photopeak window (see Fig. 10-6). The window fraction effect must be considered in specifying and comparing dead time values for systems using pulse-height analysis for energy-selective counting.

**4. Dead Time Correction Methods**

Measurements made on systems with a standardized measuring configuration, with little or no variation in window fraction from one measurement to the next, can be corrected for dead time losses using the mathematical models described in Section C.2. Some in vitro counting systems are in this category. Given an observed counting rate  $R_o$  and a dead time  $\tau$ , the true counting rate can be determined from Equation 11-17 if the system is nonparalyzable or by graphical or approximation

methods (Equation 11-18 and Fig. 11-15) if it is paralyzable.

Dead time  $\tau$  can be determined using the *two-source method*. Two radioactive sources of similar activities, for which the dead time losses are expected to be 10% to 20%, are needed (Fig. 11-16). The counting rate for source 1 is determined,  $R_1$  (cps). Without disturbing the position of source 1 (so as not to change the detection efficiency for source 1), source 2 is placed in position for counting and the counting rate for the two sources together is determined,  $R_{12}$  (cps). Then source 1 is removed (again, without disturbing source 2), and the counting rate for source 2 alone is determined,  $R_2$  (cps). If the system is non-paralyzable, the dead time  $\tau_n$  in seconds is given by

$$\tau_n \approx (R_1 + R_2 - R_{12}) / (R_{12}^2 - R_1^2 - R_2^2) \quad (11-24)$$

If the system is paralyzable, then

$$\tau_p \approx [2R_{12} / (R_1 + R_2)^2] \ln[(R_1 + R_2) / R_{12}] \quad (11-25)$$

If a short-lived radionuclide is used, decay corrections can be avoided by making the three measurements  $R_1$ ,  $R_{12}$ , and  $R_2$ , separated by equal time intervals.\*

Additional measurements are required to determine whether Equation 11-24 or 11-25 is to be used. For example, a graph of observed counting rate versus activity might be constructed to determine which of the two curves in Figure 11-15 describes the system.

For measurements in which the window fraction is variable (e.g., most in vivo measurements), the equations given in Section C.2 can be used only if the window fraction is known. Another approach is to use a

\*Some texts recommend also that a background measurement be made; however, background counting rates generally are negligibly small in comparison to the counting rates used in these tests.

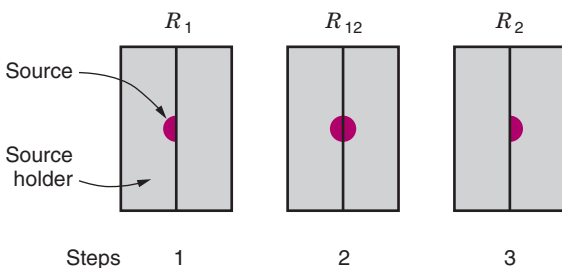


**FIGURE 11-16** Illustration of the steps followed in determining dead time by the two-source method.

fixed-rate pulser connected to the preamplifier of the radiation detector. The pulser injects pulses of fixed amplitude (usually larger than the photopeak pulses of interest) into the circuitry, and the counting rate for these events is monitored using a separate single-channel analyzer window (Fig. 11-17). The fractional loss of pulser events is equal to the fractional loss of radiation events because both are subject to the same loss mechanisms. The observed counting rate  $R_o$  from the  $\gamma$ -ray source is corrected by the ratio of true-to-observed pulser counting rates,  $P_t/P_o$ , to obtain the true  $\gamma$ -ray counting rate,

$$R_t = R_o (P_t/P_o) \quad (11-26)$$

Dead time losses also affect counting statistics. For example, the standard deviation in observed counts,  $N_o$ , is not given by  $\sqrt{N_o}$  if there are substantial dead time losses. Detailed discussions of counting statistics with dead time losses are presented in reference 7.

## D. QUALITY ASSURANCE FOR RADIATION MEASUREMENT SYSTEMS

Radiation measurement systems are subject to various types of malfunctions that can lead to sudden or gradual changes in their

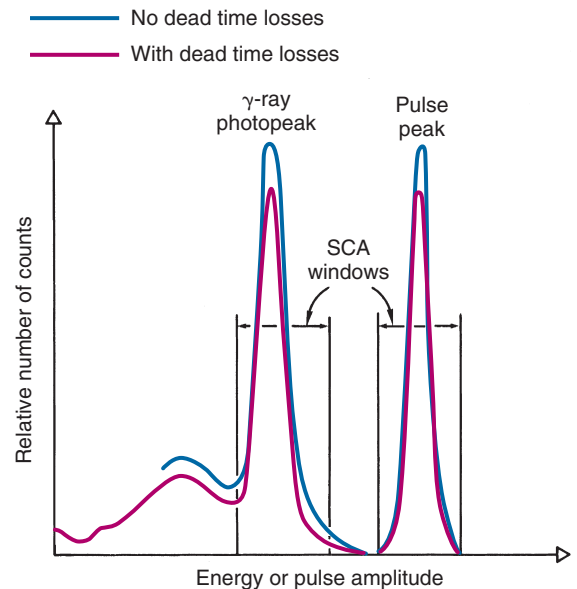


**FIGURE 11-17** Principles of dead time correction using the fixed-rate pulser method. The fractional loss of events in the pulse peak (from the fixed-rate pulser) is assumed to equal the fractional losses of radiation events in the  $\gamma$ -ray photopeak window. SCA, Single-channel analyzer.

performance characteristics. For example, electronic components and detectors can fail or experience a progressive deterioration of function, leading to changes in detection efficiency, increased background, and so forth.

To ensure consistently accurate results, *quality assurance procedures* should be employed on a regular basis for all radiation measurement systems. These would include (1) daily measurement of the system's response to a standard radiation source (e.g., a calibration "rod standard" for a well counter or a "check source" for a survey meter); (2) daily measurement of background levels; and (3) for systems with pulse-height analysis capabilities, a periodic (e.g., monthly) measurement of system energy resolution.

Additional tests may be devised to evaluate other important characteristics on specific measuring systems. The results should be recorded in a log book for analysis when problems are suspected. In some cases, it is helpful to make a graph of the results (e.g., counting rate for a standard source or for background), with tolerance limits (e.g.,  $\pm 2$  standard deviations) to detect subtle, progressive changes in performance.

The statistical tests described in Chapter 9 can be used to assist in this analysis. For example, the  $\chi^2$  test, described in Chapter 9, Section E.1, is useful for detecting sporadic

counting errors or other instabilities in system performance. Typically, a series of approximately 20 measurements are made and the  $\chi^2$  statistic is calculated. A result with  $P < 0.01$  or  $P > 0.99$  is taken as evidence of a system problem. A result with  $0.05 < P < 0.95$  is considered acceptable. A result with a  $P$  value in the gaps between these ranges is considered equivocal, and the test should be repeated.

Quality assurance procedures also are used for imaging systems as described in Chapter 14, Section E, Chapter 17, Section C.4, and Chapter 18, Section E.

## REFERENCES

1. Jaffey AH: Solid angle subtended by a circular aperture at point and spread sources: Formulas and some tables. *Rev Sci Instrum* 25:349-354, 1954.
2. NCRP Report No. 58: *A Handbook of Radioactivity Measurements Procedures*, ed 2. Bethesda, MD, 1985, National Council on Radiation Protection and Measurements, p 168.
3. Quimby EH, Feitelberg S, Gross W: *Radioactive Nuclides in Medicine and Biology*, Philadelphia, 1970, Lea & Febiger, Chapter 16.
4. Sorenson JA: Deadtime characteristics of Anger cameras. *J Nucl Med* 16:284-288, 1975.
5. Woldelessie T: Modeling of scintillation camera systems. *Med Phys* 26:1375-1381, 1999.
6. Wicks R, Blau M: The effects of window fraction on the deadtime of Anger cameras. *J Nucl Med* 18:732-735, 1977.
7. Evans RD: *The Atomic Nucleus*, New York, 1955, McGraw-Hill, pp 785-793.